Boosting Oxygen Evolution Kinetics via Sulfur/Phosphorus Dynamic Migration Induced Surface Enrichment in an Anion-Regulated Iron Selenide

Bezawit Z. Desalegn[a,b]†, Reibelle Q. Raguindin[c]†, Gaojun Jiang[a], Hyung-Ho Park[d], and Jeong Gil Seo[a,b]*

[a] *Department of Chemical Engineering, Hanyang University, Seoul 04763, Republic of Korea*

[b] *Clean-Energy Research Institute, Hanyang University, Seoul 04763, Republic of Korea*

[c] *Renewable and Sustainable Energy Research Center, Technology Innovation Institute, Abu Dhabi, United Arab Emirates*

[d] *Department of Materials Science and Engineering, Yonsei University, Seoul 03722, Republic of Korea*

**Corresponding author: +82-2-2220-0520, jgseo@hanyang.ac.kr*

† B.Z. Desalegn and R.Q. Raguindin contributed equally.

Supporting information

1. **Experimental Section**

2. **Experimental Section**

1.1. Synthesis of Electrocatalysts

Synthesis of $FeSe_2$, FeS_2 and FeP

The catalysts were synthesized following a previously reported method with some modifications [1]. Specifically, 15 mmol of NaOH and 7.5 of mmol elemental selenium powder were dissolved in 50 mL of dimethylformamide, after which 1 mL of hydrazine hydrate was added to the solution and stirred for 3 h. Then, 3.75 mmol iron nitrate nonahydrate was added to the above solution and stirred for 30 min. The mixture was transferred to a 100 mL Teflon-lined autoclave and maintained at a temperature of 180 ℃ for 12 h. After the reaction, the black precipitate was washed with deionized water and ethanol several times, respectively, and dried under vacuum at 60 ℃ for 12 h. FeS and FeP were synthesized via the same procedure using elemental sulfur and red phosphorus instead of elemental selenium.

Synthesis of anion-regulated $FeSe_2$

The S and P-regulated $FeSe_2$ were synthesized by following the same procedure as $FeSe_2$ with partial replacement of Se with S or P, respectively (Figure 1a). The as-synthesized anion-regulated catalysts are denoted as follows throughout the manuscript: S-regulated $FeSe_2$ (SR-X-$FeSe_2$) and P-regulated $FeSe_2$ (PR-X-$FeSe_2$). X denotes the mole percentage of S or P.

1.2. Electrode preparation

5 mg of electrocatalyst was added in a 0.5 mL of deionized water containing 10 μL of nafion and sonicated for 2 h. Prior to drop-casting of the electrocatalyst ink, nickel foam was ultrasonically cleaned in 1M HCl, DI water, and ethanol for 20 min each, respectively, and dried at 80 ℃ for further use. The back and front of the nickel foam was covered with epoxide resin to expose a 5 × 5 mm of geometrical area. 40 μL of the catalyst ink was drop casted on the nickel foam and dried at 60 ℃ for12 h. Four sets of electrodes were prepared per sample to obtain reproducible results.

1.3. Electrochemical Measurements

All electrochemical measurements were conducted on an SP2 ZIVE electrochemical workstation with a conventional three-electrode cell. A saturated Ag/AgCl electrode and Pt wire were used as reference and counter electrodes, respectively. The prepared aerogels loaded on nickel foam were used as the working electrode, with an exposed geometrical area of 0.5 × 0.5 cm2. All the potentials reported in this study are quoted with respect to the reversible hydrogen electrode (RHE) after 90% IR correction.

$$E_{RHE} = E_{(Ag/AgCl)} + 0.197 + 0.059pH$$

1.4. Electrocatalyst Characterization

Physico-chemical and surface analysis

X-ray powder diffraction (Bruker D8 ADVANCE X-Ray Diffractometer equipped with Cu Kα radiation (λ=0.15406 nm)) was used to study the structure of the as-prepared electrodes. The morphology and elemental distribution of the samples were studied by field emission scanning electron microscopy (FE-SEM) (FEI Verios G4 UC, Extreme High-Resolution Scanning Electron Microscope). X-ray photoelectron spectra were taken on a Thermo Scientific K-alpha plus photospectrometer using the monochromatic Al Kα source (1486.7 eV). Low-resolution survey and high-resolution region scan at the binding energies of interest were taken for each sample. The XPS depth profiling was conducted on a K-alpha plus (Thermo Scientific_USA) with a dual-beam ion source and ultra-low energy co-axial electron and Ar^+ ion beam (100eV-4 keV) and Al Ka (1486.6 eV), variable spot size (30-400μm) X-ray by using argon sputtering to reveal a new layer with a standard sputtering rate and sputtering time of 100nm/1444s for 600 s and 30s, respectively with a 30 s increment. To avoid damaging the samples during depth profiling, the spectrometer was operated in the gas cluster ion itching mode. Inductively Coupled Plasma Spectroscopy (ICP-OES) was measured using a Thermo Fisher Scientific iCAP 7400DUO ICP spectrometer. Electron paramagnetic Resonance (EPR) analysis was conducted using EMXplus-9.5/12/P/L with a magnetic field range of -13 KG-13 KG and an absolute sensitivity of $1.6*10^{-9}$ spins and a modulation frequency of 4-100 kHz (1 kHz step) at room temperature. The measurements were

conducted in the X-band at room temperature at a frequency of 9.86 GHz and a modulation frequency of 100 kHz. For EPR analysis after OER, the catalyst ink was loaded on Cu-foam to avoid magnetic interference from Ni-foam.

Catalyst-intermediate/product interaction analysis

NH_3 and O_2 TPD measurements were conducted on a MICROTRAC BELCAT catalyst analyzer. NH_3 TPD was conducted to examine the catalyst-intermediate interaction while O_2 TPD was conducted to analyze the catalyst-product interaction. For NH_3 TPD measurements, all samples were preheated at 300℃ with a heating rate of 10℃ min^{-1} for 1h to clean the surface. Afterwards, the samples were cooled to 100℃, where NH_3 (10% NH_3 in Helium) was chemisorbed for 1h. The chemisorbed NH_3 was desorbed by increasing the temperature to 900℃ with a ramping rate of 10℃ min^{-1} under the flow of pure helium.

For O_2 TPD, the samples were preheated at 150℃ under pure argon at a heating rate of 10℃ min^{-1} and kept at this temperature for 1 h. After cooling the sample to room temperature, adsorption of O_2 was carried out in flowing O_2 (5% O_2 in Argon) for 1 h at 30 ℃. Then the gas was switched to pure argon for 30 minutes. Finally, the desorption measurement was carried out by increasing the temperature to 700℃ with a heating rate of 10℃ min^{-1} under the flow of pure argon.

1.5. Quantification of Produced Oxygen

The produced oxygen was quantified using an online gas chromatography equipped with a TCD detector with argon gas as the reference. Before the start of the GC analysis, the electrochemical cell containing the electrolyte was purged with argon for 15 minutes and the reaction was conducted under a continuous flow of argon gas.

The faradaic efficiency is calculated based on the actual produced oxygen as follows.

$$\text{FE (\%)} = \frac{Actual\ oxygen\ production}{Theoretical\ oxygen\ production}$$

$$\text{Theoretical oxygen production} = \frac{I\,x\,t}{4F}$$

Where,

I = Current in A

t = time in s

F = Faraday's constant and 4 is the number of electrons required to produce one more of O_2 gas.

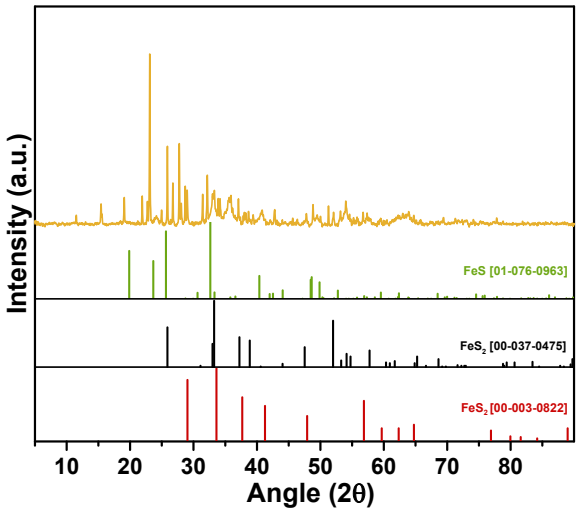

Figure S1: XRD pattern of FeS_2 with standard reference patterns.

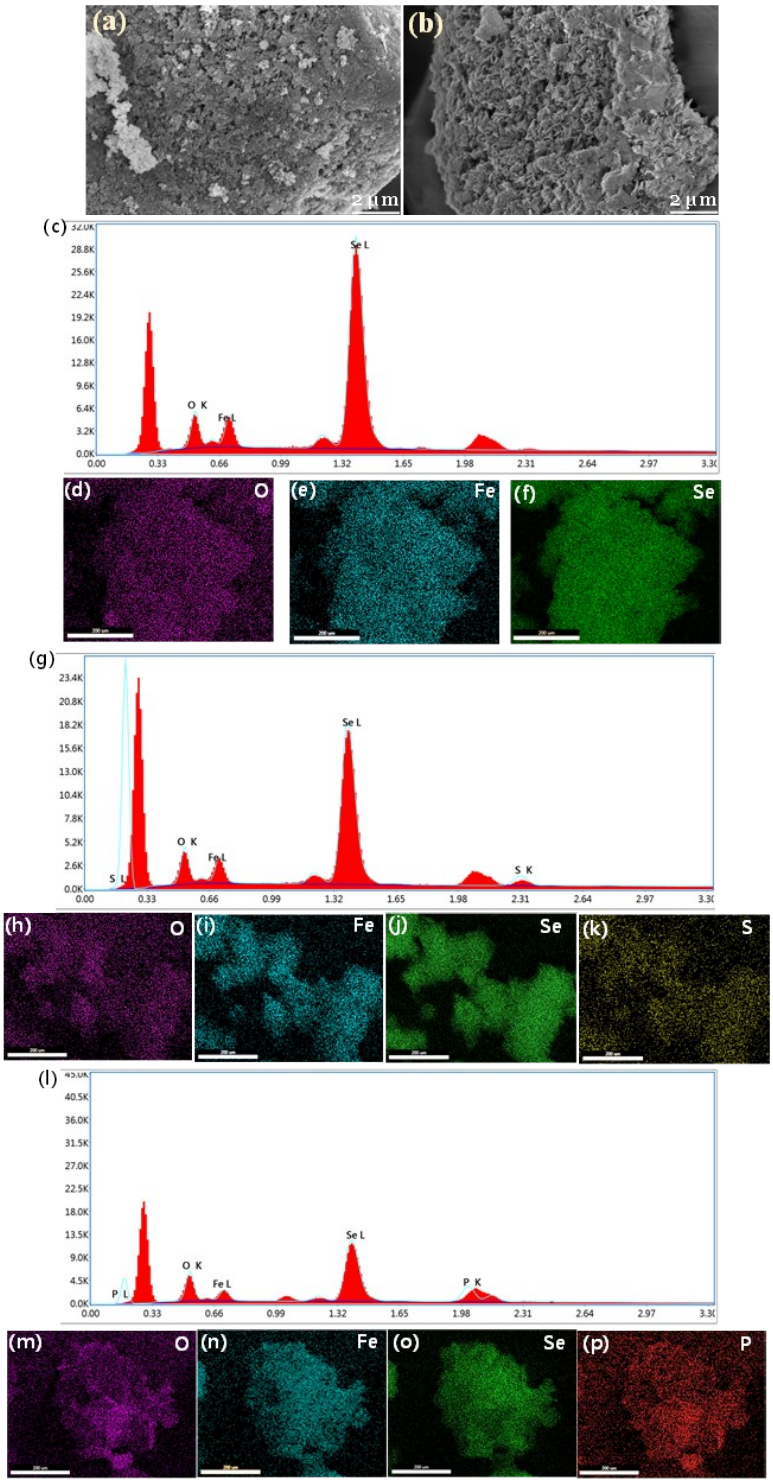

Figure S2: FE-SEM images of (a) FeP and (b) FeS_2, Elemental mappings and EDS of (c-f) $FeSe_2$, (g-k) SR-10$FeSe_2$, and (l-p) PR-30$FeSe_2$.

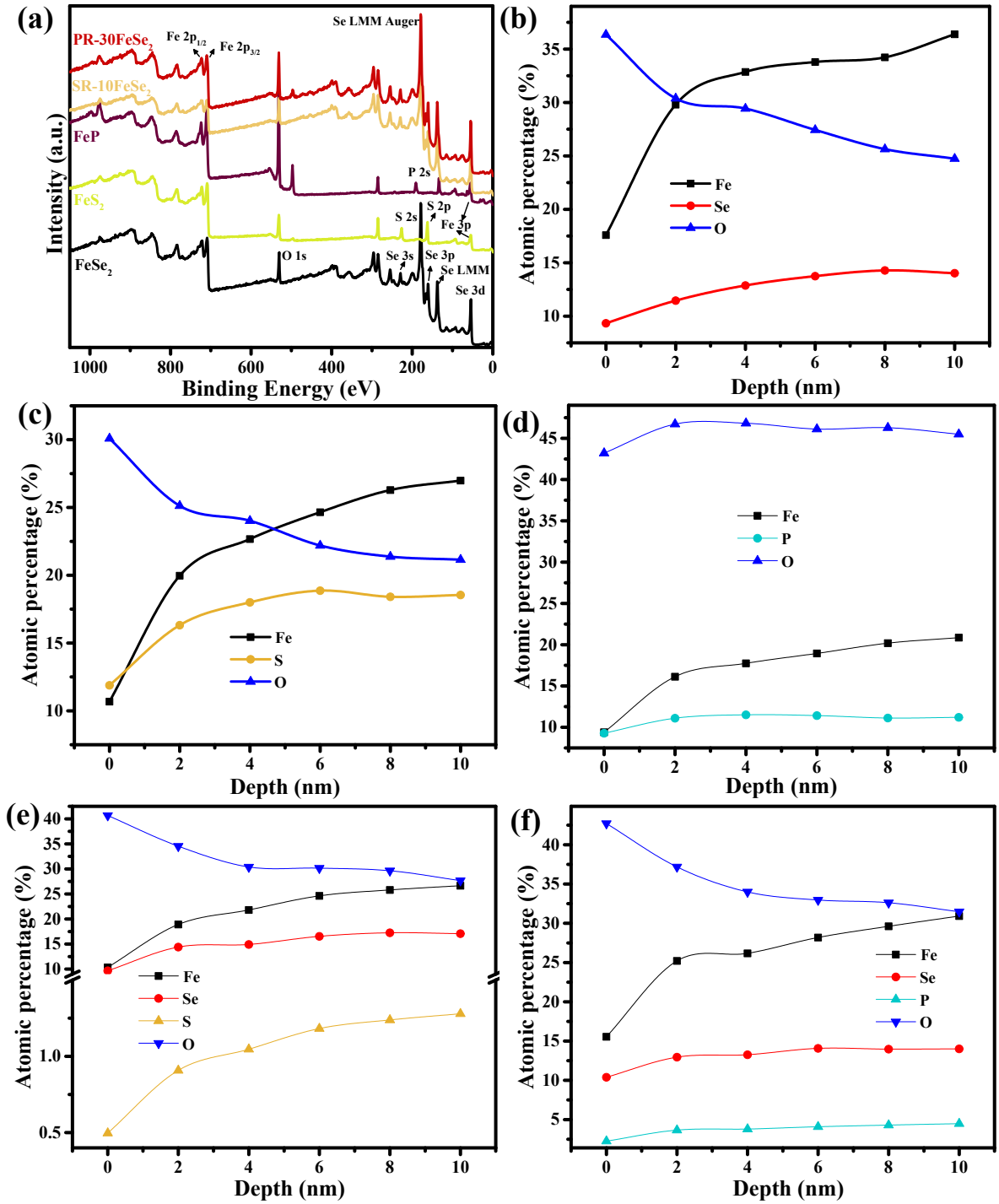

Figure S3: (a) XPS survey and atomic percentage of elements with depth (b) $FeSe_2$, (c) FeS_2, (d) FeP, (e) SR-10$FeSe_2$, and (f) PR-30$FeSe_2$.

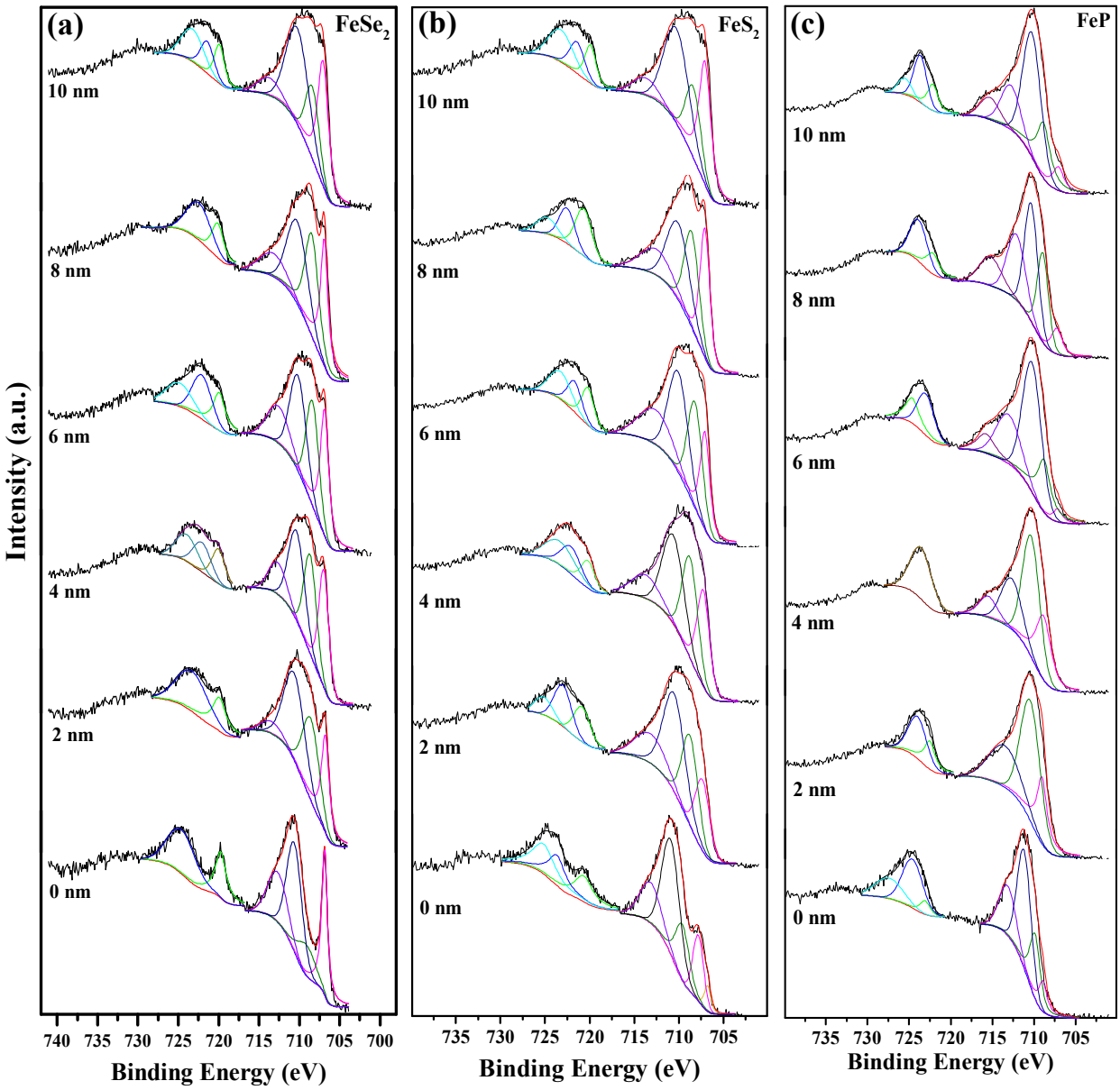

Figure S4: Fe 2p spectrums with depth; (a) $FeSe_2$, (b) FeS_2, and (c) FeP

Table S1: Mole Fractions of Fe and anions from ICP-OES analysis.

Electrocatalysts	Mole Fraction (%)			
	Fe	Se	S	P
SR-10FeSe$_2$	33	63	3	0
PR-30FeSe$_2$	34	58	0	8.4

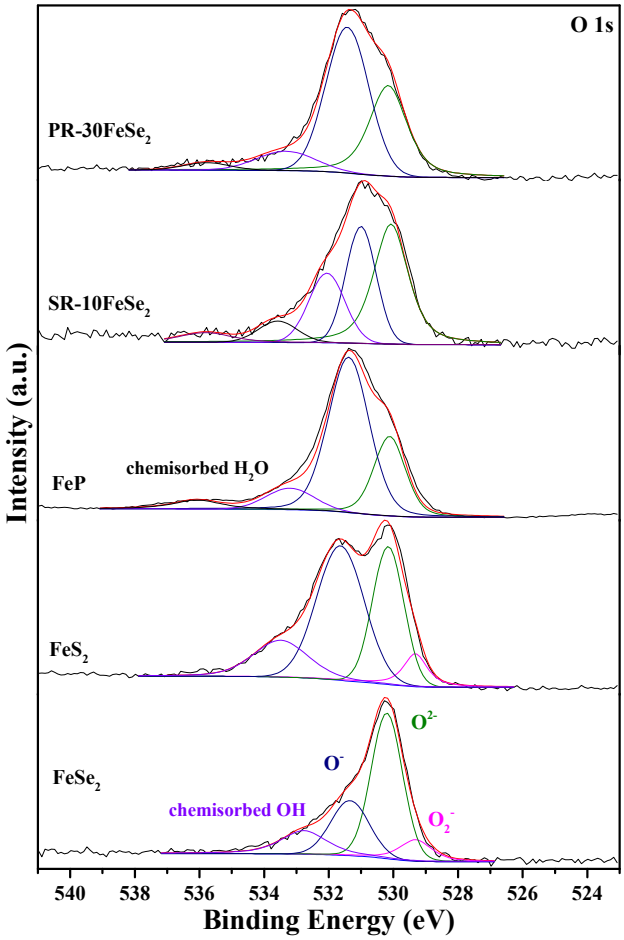

Figure S5: O 1s XPS spectrum.

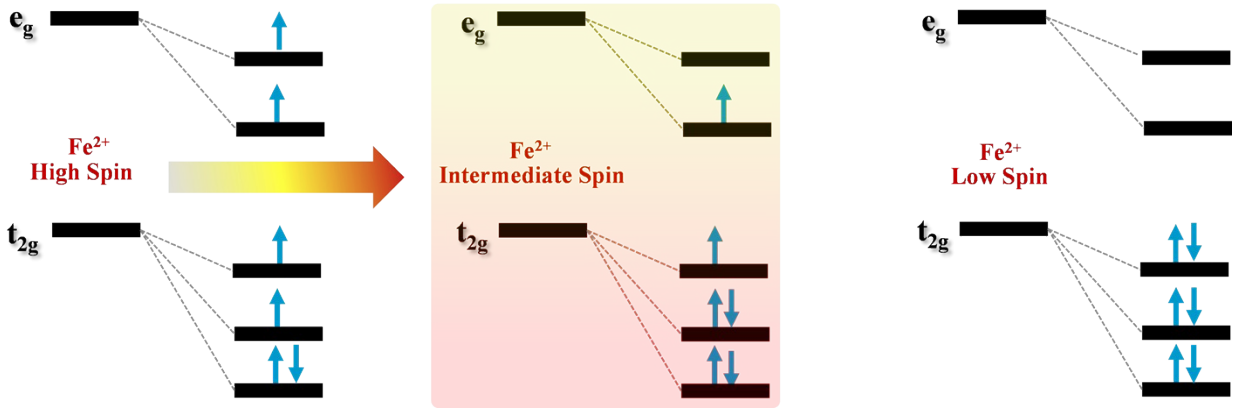

Scheme S1: Schematic illustration of transition of the change in Fe^{2+} spin state with anion-regulation.

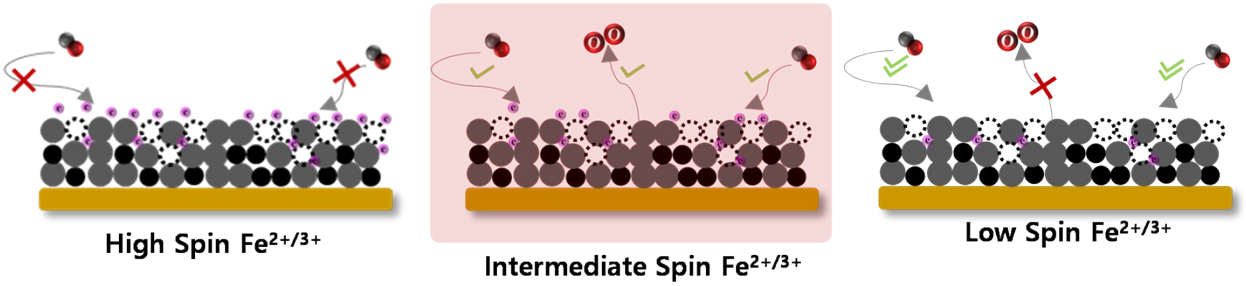

Scheme S2: Schematic illustration of the effect of e_g electrons on OER elementary steps.

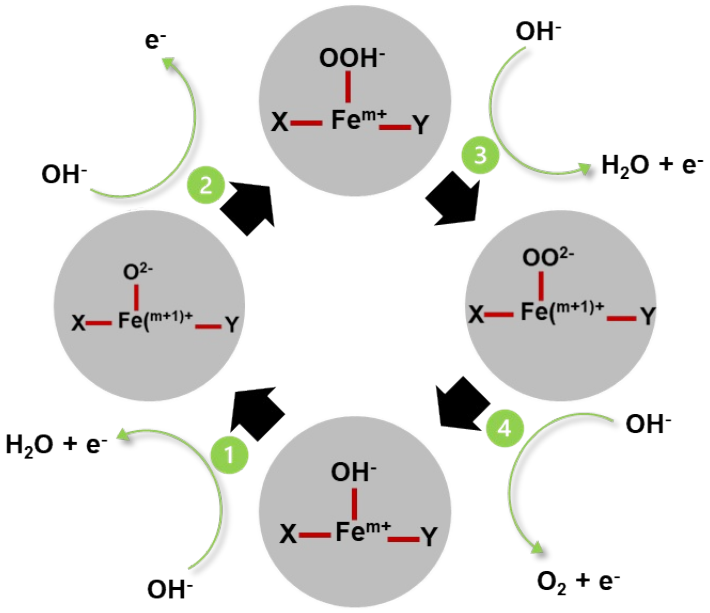

Scheme S3: Elementary steps of OER for anion-regulated $FeSe_2$. (X and Y denote Se and S/P anions, respectively)

Table S2: ICP-OES results of the electrolyte after 2h of OER.

Electrocatalysts	**Concentration (ppm)**			
	Fe	**Se**	**S**	**P**
$FeSe_2$	-	4.41	-	-
FeS_2	-	-	16.01	-
FeP	-	-	-	15.27
SR-10$FeSe_2$	-	7.16	8.71	-
PR-30$FeSe_2$	-	5.16	-	9.01

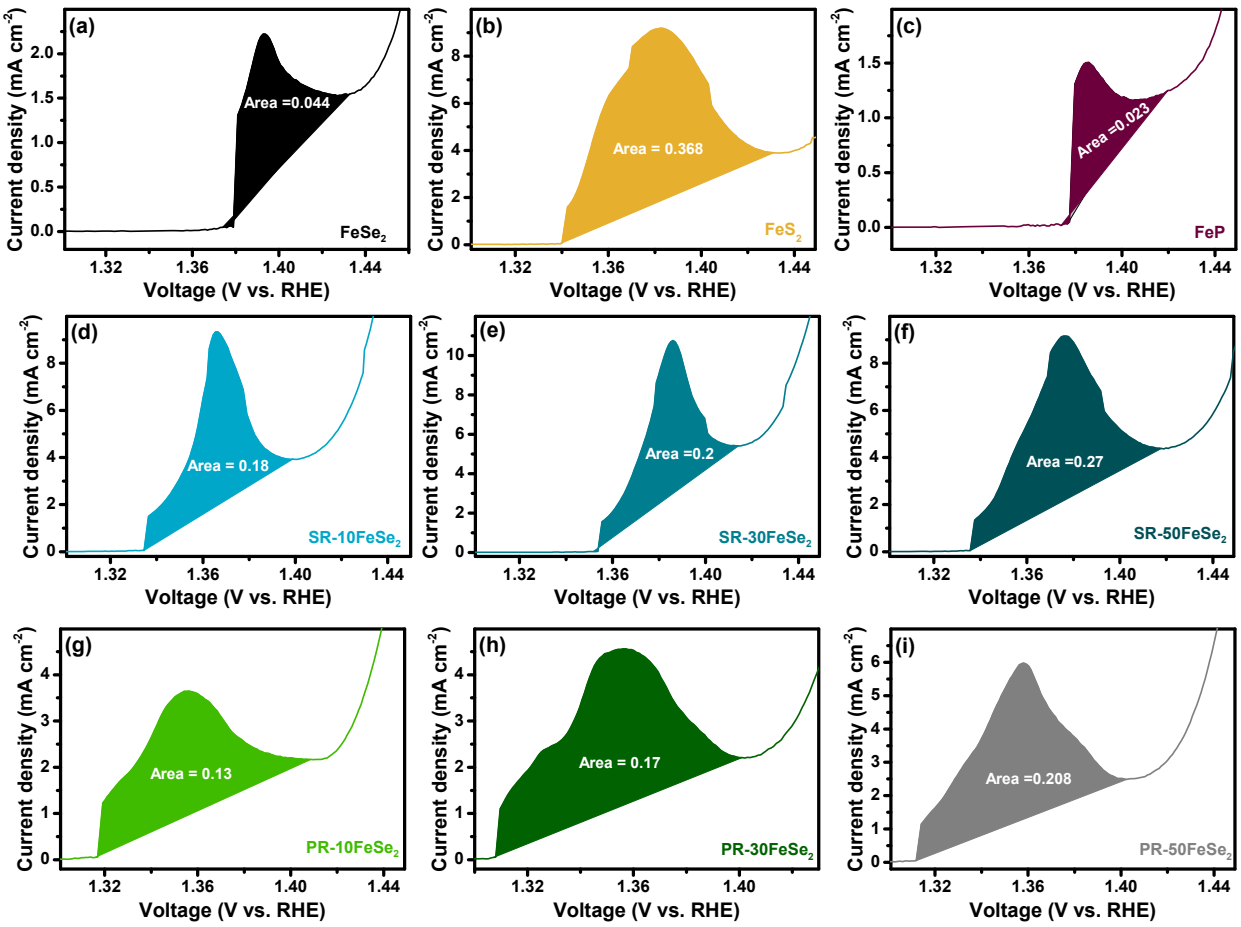

Figure S6: The integrated areas of the oxidation peak from LSVs at a scan rate of 1mV s^{-1} for all the electrodes.

"To understand the difference in performance between SR-10$FeSe_2$ and PR-30$FeSe_2$ at low and high potentials the area under the oxidation peaks at a potential of around ≈ 1.36-1.4 V vs. RHE was calculated and displayed in **Figure S6** along with the amount of generated Fe^{3+} based on the stoichiometric equation ($Fe^{2+} \leftrightarrow Fe^{3+} + e^-$) (**Figure S7).** These oxidation peaks are attributed to the formation of a high valence (Fe^{3+}) metal species prior to the onset of OER. High valence metal species are known to facilitate OH^- adsorption, however excessive Fe^{3+} (FeOOH) can result in too strong adsorption and higher charge transfer resistance. Hence, FeS_2 with the highest area and number of generated Fe^{3+} showed the lowest performance. Interestingly, SR-10$FeSe_2$ and PR-30$FeSe_2$ with an almost similar area and amount of Fe^{3+} showed similar performance, with SR-10$FeSe_2$ showing better performance at potentials lower than 1.5 V vs. RHE and PR-30$FeSe_2$ at potentials higher than 1.5 V vs. RHE. This can be explained by the facilitated OH^- adsorption on the SR-10$FeSe_2$ surface owing to a slightly higher amount of Fe^{3+} which could lead to a lower rate of OOH deprotonation at the later stage of OER (higher potential). Accordingly, the relatively lower number of Fe^{3+} on PR-30$FeSe_2$ leads to a lower affinity of OH^- at lower applied potentials

compared to the SR-10$FeSe_2$, however results in a facilitated OOH deprotonation at higher applied potentials. After reaching an optimum value, the unfavorable effect of excessive oxidation (more Fe^{3+}) is evidenced by the decline in current density and rise in overpotential (**Figures 3a and c**) with increasing Fe^{3+} (increasing S/P).

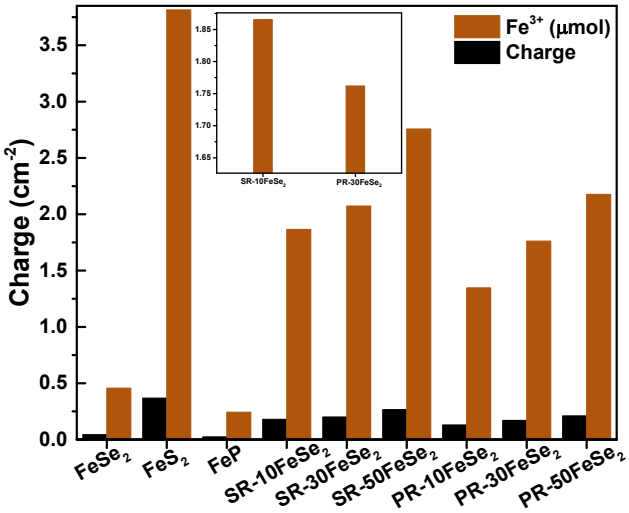

Figure S7: Calculated charge from integrated areas given in Figure S6 and amount of generated Fe^{3+}.

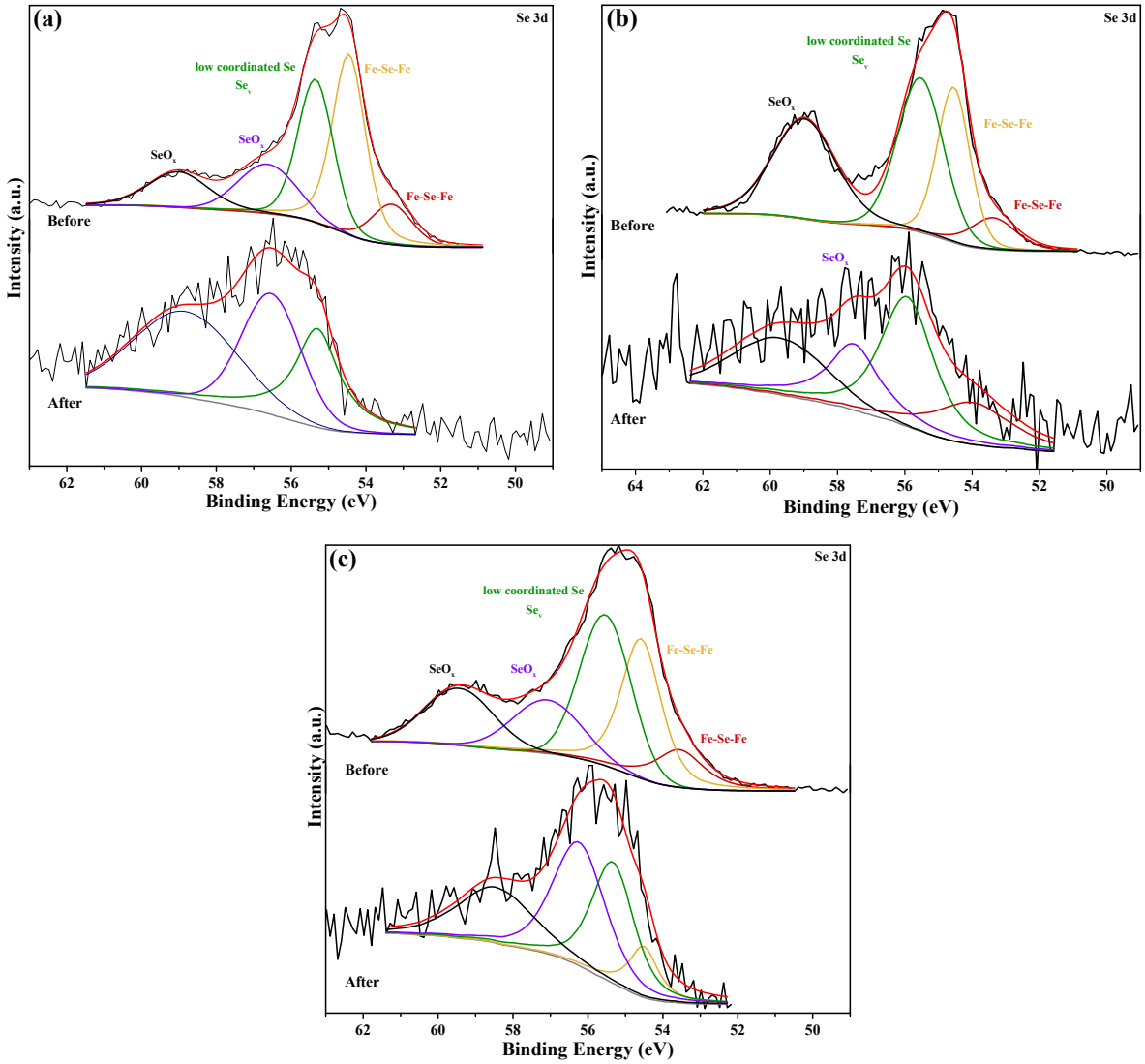

Figure S8: Se 3d spectrum before and after OER (a) $FeSe_2$, (b) SR-10$FeSe_2$ and (c) PR-30$FeSe_2$.

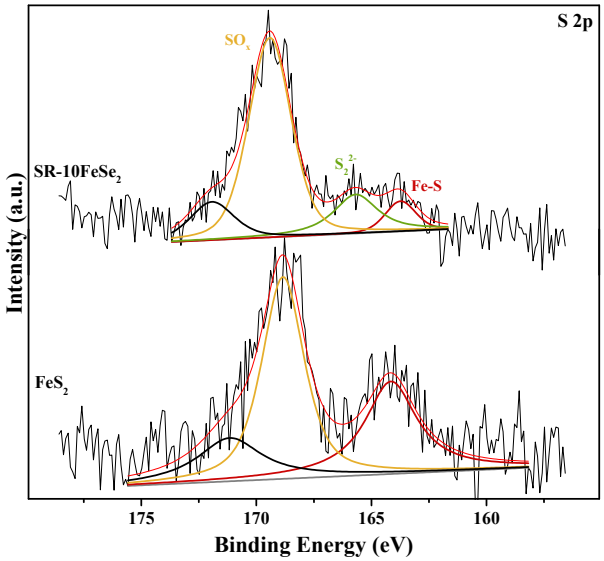

Figure S9: S 2p spectra after 2h of OER.

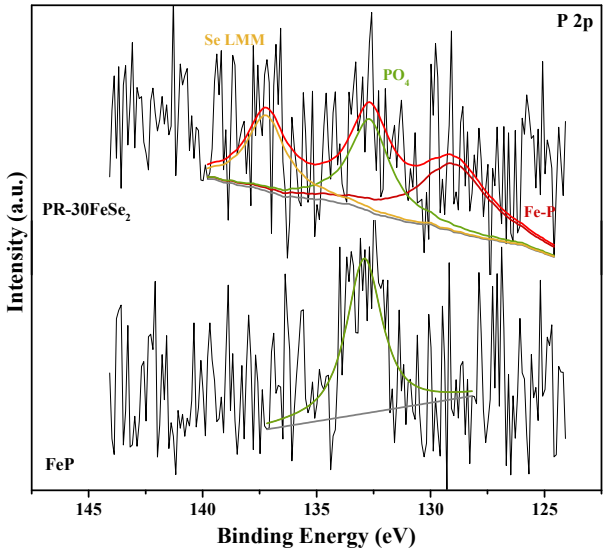

Figure S10: P 2p spectra after 2h of OER.

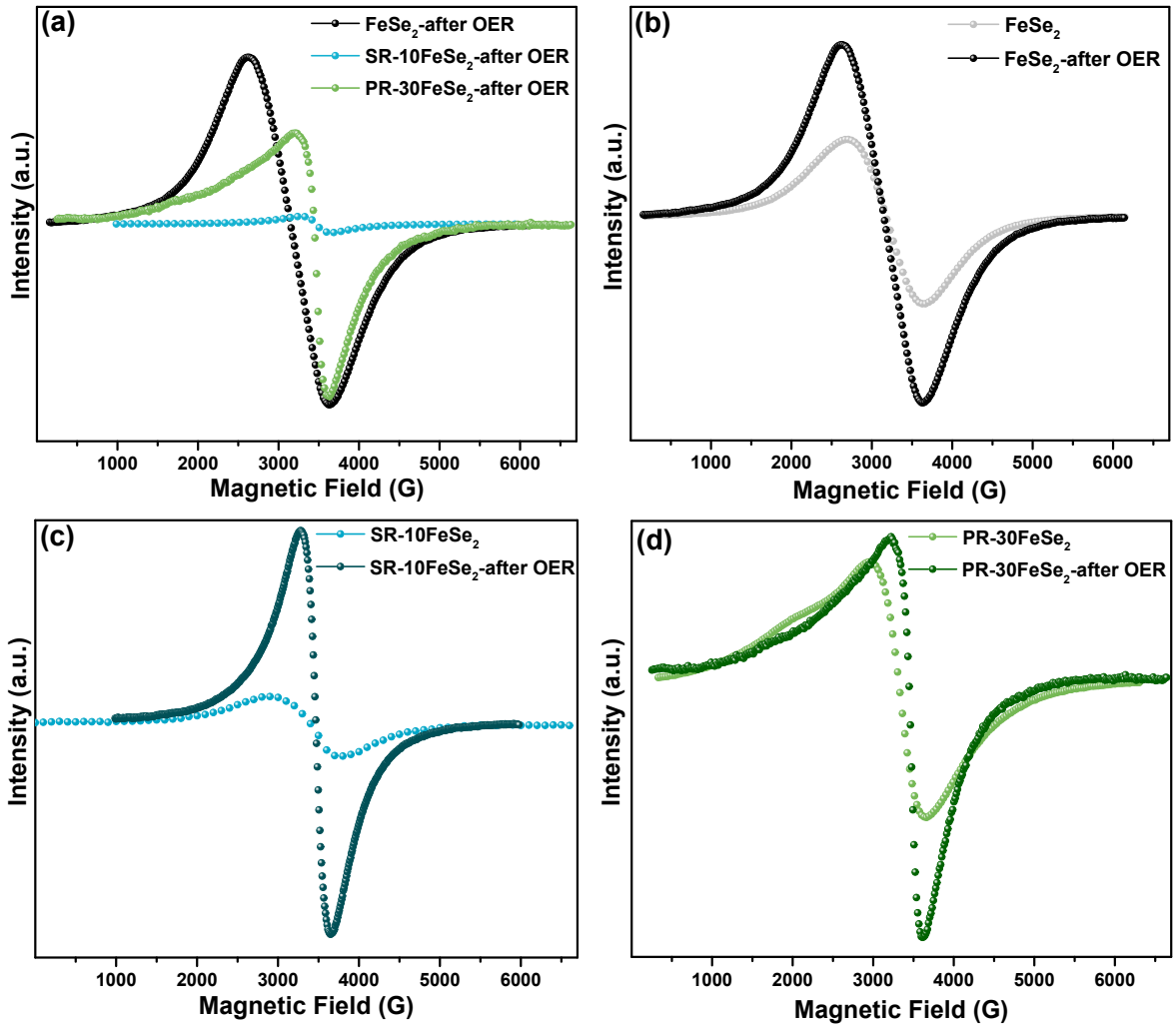

Figure S11: EPR spectra: (a) after 2h OER, before and after 2h of OER (b) $FeSe_2$, (c) SR-10$FeSe_2$, and (d) PR-30$FeSe_2$.

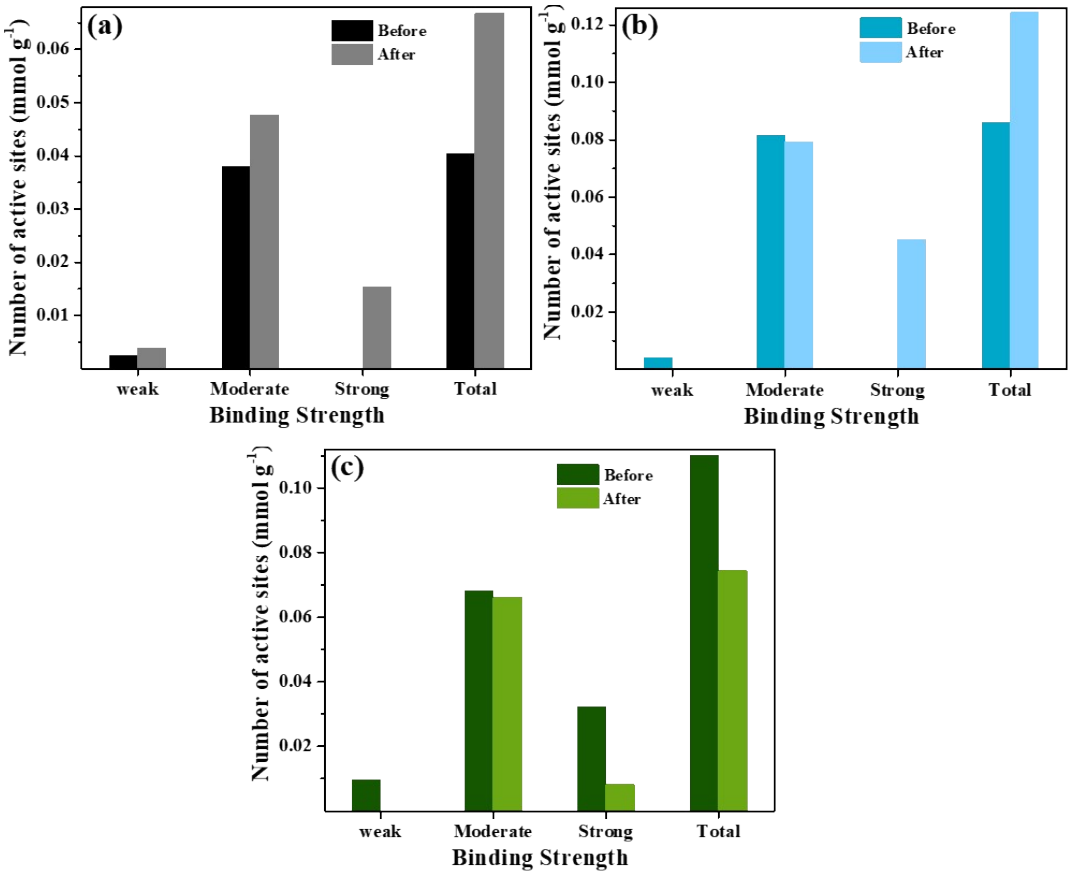

Figure S12: Number of active sites calculated from NH_3 TPD spectrum before and after 2h OER for (a) $FeSe_2$, (b) SR-10$FeSe_2$, and (c) PR-30$FeSe_2$.

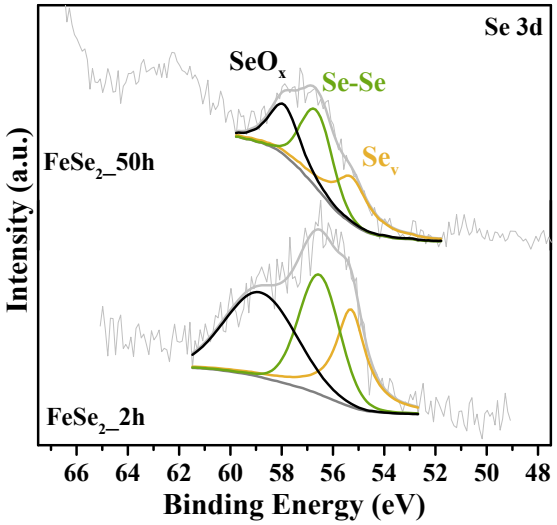

Figure S13: Se 3d spectrum of $FeSe_2$ after 2 and 50h OER.

Table S3: Performance comparison with previous reports

Electrocatalysts	Year	Overpotential @10mA cm^{-2}	References
$NiPS_3$ quantum sheets	2021	250	[2]
$NiPS_3$ Nanosheet-Graphene composite	2018	294	[3]
$Co_{0.37}S_{0.38}P_{0.02}$	2020	288	[4]
Se-Co_3S_4-$V_{S/Se}$-V_{Co}	2022	289.5	[5]
N-Ni_3S_2/NF	2017	@100-330	[6]
0.01S-$FeOOH_{+1000}$/IF	2022	@100-254	[7]
Se/Fe-Co_9S_8-0.14	2020	298	[8]
Se_x-Co_3S_4	2022	289	[5]
$FePSe_3$	2018	740	[9]
Mn-Co oxyphosphide	2017	370	[10]
$FeCoO_x$-V_o-S	2020	250	[11]
NiFe(Oxy)Sulfide	2017	286	[12]
$Co_3FeS_{1.5}(OH)_6$	2017	358	[13]
CoMnON	2016	470	[14]
CoFePO	2016	333	[15]
P-Co_3O_4	2017	280	[16]
FeNiSeO	2021	257	[17]
S-Ni_3Se_4-2	2021	275	[18]
SR-10$FeSe_2$		**212 @600-290**	**This work**
PR-30$FeSe_2$		**223 @600-275**	**This work**

References

1 B. Z. Desalegn, K. Hern and J. Gil Seo, *ChemCatChem*, , DOI:10.1002/cctc.202100969.

2 K. Huang, Y. Xu, Y. Song, R. Wang, H. Wei, Y. Long, M. Lei, H. Tang, J. Guo and H. Wu, *J. Mater. Sci. Technol.*, 2021, **65**, 1–6.

3 S. Xue, L. Chen, Z. Liu, H. M. Cheng and W. Ren, *ACS Nano*, 2018, **12**, 5297–5305.

4 S. Liu, C. Che, H. Jing, J. Zhao, X. Mu, S. Zhang, C. Chen and S. Mu, *Nanoscale*, 2020, **12**, 3129–3134.

5 X. Gu, S. Li, W. Shao, X. Mu, Y. Yang, Y. Ge, W. Meng, G. Liu, S. Liu and S. Mu, *Small*, 2022, **18**, 1–7.

6 P. Chen, T. Zhou, M. Zhang, Y. Tong, C. Zhong, N. Zhang, L. Zhang, C. Wu and Y. Xie, *Adv. Mater.*, 2017, **29**, 1–6.

7 X. Y. Zhang, F. T. Li, Y. W. Dong, B. Dong, F. N. Dai, C. G. Liu and Y. M. Chai, *Appl. Catal. B Environ.*, 2022, **315**, 121571.

8 D. Zhang, J. Zhang, X. Fu, J. Pan and Y. Wang, *Nanotechnology*.

9 D. Mukherjee, P. Muthu Austeria and S. Sampath, *ACS Appl. Energy Mater.*, 2018, **1**, 220–231.

10 B. Y. Guan, L. Yu and X. W. D. Lou, *Angew. Chemie - Int. Ed.*, 2017, **56**, 2386–2389.

11 L. Zhuang, Y. Jia, H. Liu, Z. Li, M. Li, L. Zhang, X. Wang, D. Yang, Z. Zhu and X. Yao, *Angew. Chemie - Int. Ed.*, 2020, **59**, 14664–14670.

12 B. Q. Li, S. Y. Zhang, C. Tang, X. Cui and Q. Zhang, *Small*, 2017, **13**, 1–6.

13 H. F. Wang, C. Tang, B. Wang, B. Q. Li and Q. Zhang, *Adv. Mater.*, 2017, **29**, 1–9.

14 Y. Li, K. A. Kuttiyiel, L. Wu, Y. Zhu, E. Fujita, R. R. Adzic and K. Sasaki, *ChemSusChem*, 2017, **10**, 68–73.

15 J. Duan, S. Chen, A. Vasileff and S. Z. Qiao, *ACS Nano*, 2016, **10**, 8738–8745.

16 Z. Xiao, Y. Wang, Y. C. Huang, Z. Wei, C. L. Dong, J. Ma, S. Shen, Y. Li and S. Wang, *Energy Environ. Sci.*, 2017, **10**, 2563–2569.

17 L. Zhang, C. Lu, F. Ye, Z. Wu, Y. Wang, L. Jiang, L. Zhang, C. Cheng, Z. Sun and L. Hu, *Appl. Catal. B Environ.*, 2021, **284**, 119758.

18 K. Wan, J. Luo, X. Zhang, P. Subramanian and J. Fransaer, *J. Energy Chem.*, 2021, **62**, 198–203.